Interfacial antiferromagnetic coupling driven magnetotransport properties in ferromagnetic superlattices

Sandip Halder,[1] Subrat K. Das [○],[2] and Kalpataru Pradhan[1,*]

[1]*Theory Division, Saha Institute of Nuclear Physics, A CI of Homi Bhabha National Institute, Kolkata 700064, India*
[2]*SKCG Autonomous College, Paralakhemundi, Odisha 761200, India*

We explore the role of interfacial antiferromagnetic interaction in coupled soft and hard ferromagnetic layers to ascribe the complex variety of magnetotransport phenomena observed in $La_{0.7}Sr_{0.3}MnO_3/SrRuO_3$ (LSMO/SRO) superlattices (SLs) within a one-band double-exchange model using Monte Carlo simulations. Our model Hamiltonian incorporates magnetocrystalline anisotropy interactions and superexchange interactions of the constituent materials, and two types of antiferromagnetic interactions between Mn and Ru ions at the interface: (i) carrier-driven and (ii) Mn–O–Ru bond superexchange to investigate the properties along hysteresis loop. We find that the antiferromagnetic coupling at the interface induces LSMO and SRO layers to align in antiparallel orientation at low temperatures. Our results reproduce the positive exchange bias of the minor hysteresis loop of LSMO/SRO SL at low temperatures, as reported in experiments. In addition, conductivity calculations show that the carrier-driven antiferromagnetic coupling between the two ferromagnetic layers steers the SL towards a metallic (insulating) state when LSMO and SRO are aligned in antiparallel (parallel) configuration, in good agreement with the experimental data. This demonstrates the necessity of carrier-driven antiferromagnetic interactions at the interface to understand the one-to-one correlation between magnetic and transport properties observed in experiments. For high temperature, just below the ferromagnetic T_C of SRO, we unveil the unconventional three-step flipping process along the magnetic hysteresis loop. We emphasize the key role of interfacial antiferromagnetic coupling between LSMO and SRO to understand these multiple-step flipping processes along the hysteresis loop.

I. INTRODUCTION

Transition-metal oxides, particularly those with the perovskite structure, are materials of great interest due to both their basic physics [1,2] and potentiality in technological applications [3–5]. They exhibit a wide variety of collective, coupled complex magnetic behaviors in bulk form [2,6,7]. Unique physics emerges from bilayers of two such materials which are believed to be among the potential optimal heterostructures for future technological spintronics applications [8–11]. It is generally agreed upon that the interface decides the coupling between the layers and the overall properties of the heterostructure [12–16]. Magnetic order at interfaces often drives the magnetism of constituent materials in bilayers [4,17]. Some of the key features that originate due to the magnetic reconstructions at the interface are unusual tunneling magnetoresistance [18], inverse spin-Hall effect [19,20], exchange bias (EB) [21–24], etc.

The EB effect is one of the most widely studied interface phenomena observed in many magnetic materials and heterostructures [25–31]. Stronger interfacial interaction can change the magnetic response of a heterostructure dramatically as compared to its constituent counterparts [16,32,33]. In the case of coupled soft/hard ferromagnetic heterostructures

with very different coercive fields, the magnetization of the softer ferromagnet (FM) can selectively be 'twist' with respect to the harder FM during magnetic hysteresis measurements [34]. The interfacial interaction has the ability to shift the magnetic hysteresis loop, making it asymmetric about the zero applied field. This feature, known as the EB effect, is extensively used to pin the magnetization of hard FMs. The shift of the magnetization loop in the direction of (opposite to) applied bias field is referred to as positive (negative) EB. In case of positive EB, the interfacial exchange interaction is believed to be antiferromagnetic [23]. EB-induced pinning of magnetization of one magnetic layer has significant potential applications in spin valves [34,35], magnetic recording read heads [36], magnetic random access memory circuits [37], giant magnetoresistive sensors [38], etc.

Thin film heterostructures of hard and soft FMs are of great interest for realization of EB, which also lead to the appearance of the very interesting phenomenon of an inverted hysteresis loop (IHL) [39–41]. In a hysteresis loop, generally, the remanence is found to be positive with magnetization M oriented along applied field h when one reduces the field strength to zero from it's saturation value. On the other hand, in case of IHL, the magnetization is found to be aligned along the opposite direction to applied field h, when still $h > 0$. As a result, an IHL showcases a negative coercivity and negative remanence. Such an anomalous behavior of the magnetization M-h curve is observed in amorphous Gd–Co films [42],

*kalpataru.pradhan@saha.ac.in

bulk ferrimagnet of composition Er_2CoMnO_6 [43], exchange coupled multilayers [44], hard/soft multilayers [45,46], and single domain particles with competing anisotropies [47].

Ferromagnetic half-metallic manganites are considered to be good candidates for engineering spintronics devices. Particularly, heterostructures comprised of LSMO as one of the constituent materials such as LSMO/SRO [48,49], LSMO/$BiFeO_3$ [50], and LSMO/$La_{0.7}Sr_{0.3}CoO_3$ [51] have been extensively studied in the last decades. Especially, LSMO and SRO are attractive materials due to their epitaxial growth and lattice-matched heterostructures, which show several interface-driven interesting magnetic phenomena [52–56]. LSMO is a well-studied half-metallic FM [57–59], whereas SRO is a rare $4d$-based oxide having ferromagnetic ordering [60,61]. In the recent past, the temperature dependence of the magnetization reversal mechanism has also been investigated in perovskite ferromagnetic oxide's superlattices (SLs), LSMO/SRO [62]. The interplay of interlayer exchange coupling and magnetocrystalline anisotropy results in an inverted hysteresis loop at low temperatures. In addition, at higher temperature (close to the T_C value of SRO), the SL shows an unconventional triple-flip mechanism (LSMO ↑ SRO ↑ to LSMO ↑ SRO ↓ to LSMO ↓ SRO ↑ to LSMO ↓ SRO ↓), where the SRO layer switches first on reducing the magnetic field from saturation value [62]. This ferrimagnetic SL configuration flips its alignment for magnetic field of opposite polarity, and later both the layers align along the external magnetic field. So, the underlying flipping mechanism in LSMO/SRO SL makes it a suitable model system for theoretical investigations. In fact, a microscopic description to understand the multiple-flipping processes in LSMO/SRO SLs is warranted.

In this paper, our aim is to present a qualitative understanding of the underlying mechanism of experimentally observed EB, IHL, and the unconventional triple-flip behavior of LSMO/SRO SLs [62], emphasizing the role of interlayer antiferromagnetic couplings [56,63]. To investigate these interesting temperature-dependent magnetizations along with transport properties, we construct a model Hamiltonian for the LSMO/SRO like SL systems and employ the Monte-Carlo technique based on traveling cluster approximation (TCA) for handling large size systems [64,65]. We observe the EB and IHL at low temperature and the unconventional triple-flip behavior of magnetic hysteresis loops at high temperature similar to the experiments. We find that a stronger interlayer antiferromagnetic coupling is necessary to realize the multiple flip nature of the hysteresis curve. The antiferromagnetic interactions at the interface gains strength from both carrier-driven and bond-driven interactions between Mn and Ru ions. But, the carrier-driven antiferromagnetic interaction at the interface is necessary to understand the one-to-one correspondence between magnetic and transport properties observed in LSMO/SRO SLs.

The organization of the paper is as follows: In the next section, we present the electronic structures and the relevant properties of constituent materials (LSMO and SRO), and the nature of the interfacial coupling in their SL configuration. In Sec. III, we introduce a suitable model Hamiltonian and the methodology to solve the SL systems, while Sec. IV establishes the parameter values for the constituent bulk
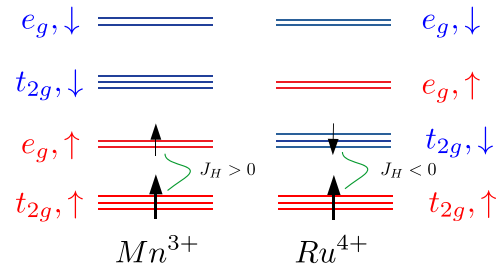

FIG. 1. The energy band diagrams of $3d$ orbitals of Mn^{3+} ions in LSMO (in left panel) and $4d$ orbitals of Ru^{4+} ions in SRO (in right panel) are schematically shown. The Hund's coupling constant J_H between majority core spins and minority spin is positive for Mn^{3+} ions and negative for Ru^{4+} ions. The spacing of energy levels are not drawn to scale.

materials by reproducing their essential properties qualitatively. In Sec. V, we start our SL calculations by exhibiting the fact that LSMO and SRO layers align antiferromagnetically at low temperatures, which triggers an insulator-metal transition with decreasing temperature. In Secs. VI and VII, we present the underlying mechanism of EB and IHL, respectively, as observed in low-temperature experiments. Then, we discuss the more unconventional high-temperature three-step switching process of the magnetic hysteresis loop in LSMO/SRO SLs and emphasize the role of interfacial antiferromagnetic coupling in Sec. VIII. Section IX summarizes our key findings.

II. ELECTRONIC STRUCTURES OF CONSTITUENT MATERIALS

In this section, we discuss the relevant properties of constituent layers in LSMO/SRO SL. LSMO is the optimally doped compound of $LaMnO_3$ with Sr in place of La, where three $3d$ valence electrons of Mn ion are occupied in t_{2g} orbitals and the e_g orbitals remain partially filled [66,67]. The average electron density $n = 0.7$ is defined on the basis of occupancy of e_g electrons. Three electrons in the t_{2g} orbitals form a large core spin. We consider it as classical spin [68] **S** and fix $|\mathbf{S}| = 1$, which is coupled to the itinerant e_g electron spin via the Hund's coupling [68–71]. Delocalization of e_g electrons results in a ferromagnetic metallic state in the double-exchange limit. Here, we assign Hund's coupling to be large and positive, where itinerant electrons are aligned along the core spins (3 ↑, 1 ↑) as shown in Fig. 1. This high-spin configuration forms a total moment $\sim 3.7 \mu_B$ as reported in experiments [72]. Also, it is observed that LSMO has a relatively high ferromagnetic transition temperature ($T_C \sim 360$ K), negligible magnetic anisotropy, and low coercive field [73].

Coming to the next material, $SrRuO_3$ (SRO) is believed to be an itinerant FM with finite density of states at the Fermi level [74]. Here, Ru is in the Ru^{4+} state and all $4d^4$ electrons are occupied in t_{2g} orbitals (3 ↑, 1 ↓), forming a low spin configuration state of total moment $2\mu_B$, which is close to the experimentally observed value $\sim 2.2\mu_B$ [75]. Other experimental reports suggest that the Ru^{4+} ion moment in SRO varies wildly, depending upon the growth conditions, and

found to be between 1.0–1.6 μ_B [76–80]. It is also known that compressively strained films exhibit enhanced saturated magnetic moments [61]. A lower value of the magnetic moment indicates the itinerant nature of t_{2g} electrons. But, the coexistence of localized and itinerant magnetism cannot be ruled out completely [81–83]. In our model Hamiltonian approach, we consider 3 ↑ electrons as localized classical spin **S** which is Hund's coupled to the ↓ itinerant electrons with an average system electron density $n = 0.5$ that give rise to an effective moment $\sim 2.5\mu_B$ [75,84]. The sign of the Hund's coupling constant of low spin state t_{2g} electrons in SRO is of opposite sign to that we assigned in LSMO (schematically shown in Fig. 1). Although both LSMO and SRO have metallic conductivity at low temperatures, SRO is a relatively bad metal [85,86] and the ferromagnetic transition temperature of SRO $T_C^{\mathrm{SRO}} \sim 160$ K [76,87], which is much smaller than that of LSMO. Experimental observations show that SRO has larger magnetic anisotropy and higher coercive field in comparison to LSMO [76,88,89]. As a result, LSMO is the most preferred candidate for soft magnetic materials when coupled with hard FM like SRO, which has a relatively larger coercive field [39,56].

Based on the above facts, where itinerant electrons are polarized in the opposite direction (parallel) to that of the localized t_{2g} core spins in SRO (LSMO), it is clear that the itinerant electrons prefer antiferromagnetic alignment (over ferromagnetic alignment) of Mn and Ru t_{2g} core spins at the interface to facilitate hopping and gain kinetic energy [84]. As a result, the interfacial hopping drive the system to be less resistive in the antiferromagnetic configuration between the constituents ferromagnetic layers as compared to the ferromagnetic or paramagnetic configuration, in agreement with experiments [90]. This shows that carrier-driven antiferromagnetic interaction is necessary to understand the one-to-one correspondence between magnetic and transport properties of LSMO/SRO SLs along the hysteresis loop. It is worthwhile to note that in addition to this carrier-driven coupling, the interfacial Mn–O–Ru bonds also generate a stronger antiferromagnetic superexchange coupling at the interface [56,63], which is also need to be incorporated.

III. MODEL HAMILTONIAN AND METHODS

With the backdrop of electronic structures, we construct a reference one-band classical Kondo lattice model Hamiltonian [70,71,91] in three dimensions to investigate LSMO/SRO SLs as follows:

$$H = -t \sum_{<ij>,\sigma} (c_{i\sigma}^{\dagger} c_{j\sigma} + \mathrm{H.c.}) - J_H \sum_i \mathbf{S}_i.\sigma_i$$
$$+ J \sum_{<ij>} \mathbf{S}_i.\mathbf{S}_j - A_{\mathrm{aniso}} \sum_i (S_i^z)^2$$
$$- \mu \sum_{i\sigma} c_{i\sigma}^{\dagger} c_{i\sigma} + \sum_{i\sigma} \epsilon_i c_{i\sigma}^{\dagger} c_{i\sigma}.$$

Here, the operator $c_{i\sigma}$ ($c_{i\sigma}^{\dagger}$) annihilates (creates) an itinerant electron with spin σ_i at site i. J_H is the Hund's coupling between the t_{2g} spins $\mathbf{S_i}$ and the itinerant electron spin σ_i. We treat $\mathbf{S_i}$ to be classical variable and fix $|\mathbf{S_i}| = 1$. J is the antifer-

romagnetic superexchange between the classical $\mathbf{S}_i$ spins and A_{aniso} is the strength of magnetocrystalline anisotropy. Chemical potential μ is tuned to set the average electron density of the overall system. ϵ_i is the on-site potential, essential for layered systems to keep the electron densities of both layers at their desired values. This term can be neglected for bulk systems. We perform our calculations in an external magnetic field h by adding the Zeeman coupling $-\mathbf{h} \cdot \sum_i \mathbf{S}_i$ to the Hamiltonian.

We apply the exact diagonalization scheme to the itinerant electrons in the configuration of a fixed background of classical spins. The classical variables are annealed by a Monte Carlo procedure at each site where the proposed update is accepted or rejected by using the Metropolis algorithm starting with the random initial configuration. At each temperature, we use 2000 system sweeps for annealing and in each sweep every lattice site is visited sequentially and updates the system. We measure physical observables like magnetization after thermalizing the system at each ten sweeps to avoid illicit self-correlation in the data. To access larger system sizes, we use TCA [64,65] based Monte Carlo scheme. We set up our calculations for m-LSMO/n-SRO SLs in 3D (N = $10 \times 10 \times 8$). Here, $m(n)$ represents the number of LSMO (SRO) planes with $m + n = 8$. The size of the TCA cluster is taken to be $4 \times 4 \times 8$. From now onward, we assign different SL structures as m/n SL, where m LSMO planes constitute the LSMO layer and n SRO planes constitute the SRO layer. To establish the bulk properties of individual LSMO and SRO layers, we use $8 \times 8 \times 8$ system size.

IV. PARAMETER VALUES TO MIMIC PROPERTIES OF BULK LSMO AND SRO

To capture the essential physics of individual LSMO and SRO layers qualitatively, it is necessary to explore and find out two different sets of parameter values comprising t, J_H, J_{SE}, and A_{aniso}. Keeping the basic properties of the constituent materials in mind, first we consider to build up the parameter space for LSMO. We set $t_{\mathrm{Mn}} = 1$ and calculate all the observables in the unit of t_{Mn}. To mimic the ferromagnetic metallic state, the Hund's coupling constant is set in the double-exchange limit, $J_H^{\mathrm{Mn}} = 24$. We add a small antiferromagnetic superexchange interaction, putting $J_{\mathrm{SE}}^{\mathrm{Mn}} = 0.01$, and neglect the magnetocrystalline anisotropy ($A_{\mathrm{aniso}}^{\mathrm{LSMO}} = 0$), which is much smaller than the SRO system.

Now, for SRO the parameters must be chosen in such a way that its physics relative to LSMO remain intact at least qualitatively, e.g., the transition temperature $T_C^{\mathrm{SRO}} < T_C^{\mathrm{LSMO}}$, the coercive field $H_C^{\mathrm{SRO}} > H_C^{\mathrm{LSMO}}$, etc. Hence, we choose the hopping parameter $t_{\mathrm{Ru}} = 0.5$, the Hund's coupling $J_H^{\mathrm{Ru}} = -12$, and the magnetocrystalline anisotropy interaction $A_{\mathrm{aniso}}^{\mathrm{SRO}} = 0.05$. The modality by which we assign a negative sign to J_H^{Ru} is already discussed in Sec. II (please see the discussion related to Fig. 1). A finite $A_{\mathrm{aniso}}^{\mathrm{SRO}}$ is essential to capture the higher value of coercive field H_C in SRO compared to LSMO at low temperatures. We neglect any kind of superexchange interaction in SRO. The electron densities are already fixed from the electronic structures of both materials, $n \sim 0.7$ for LSMO and $n \sim 0.5$ for SRO, as outlined earlier. We tabulate

TABLE I. Various parameters to model LSMO- and SRO-like systems. For LSMO/SRO SLs, we set $J_I = 0$ and $t_I = 0.75$ unless otherwise mentioned.

System	Parameters to mimic LSMO- and SRO-like systems
LSMO	$n = 0.7$, $J_H^{Mn} = 24$, $t_{Mn} = 1$, $J_{SE}^{Mn} = 0.01$, $A_{aniso}^{LSMO} = 0$
SRO	$n = 0.5$, $J_H^{Ru} = -12$, $t_{Ru} = 0.5$, $J_{SE}^{Ru} = 0$, $A_{aniso}^{SRO} = 0.05$

the parameter sets for LSMO-like and SRO-like materials in Table I.

The next task is to calculate and establish the essential properties of LSMO-like and SRO-like materials separately, using the parameter sets given in Table I. We present the magnetization $M = 1/N \sum_i S_i^z$ data in Fig. 2(a), where N is number of sites and S^z is the z component of the classical spins. The magnetization versus temperature graphs show that the ground state is ferromagnetic for both materials with $T_C^{LSMO} > T_C^{SRO}$. In experiments, T_C^{LSMO} is measured to be as large as twice of T_C^{SRO}. We agree that our calculations do not reflect this fact quantitatively. It is important to note here that the magnetocrystalline anisotropy is mainly a low temperature
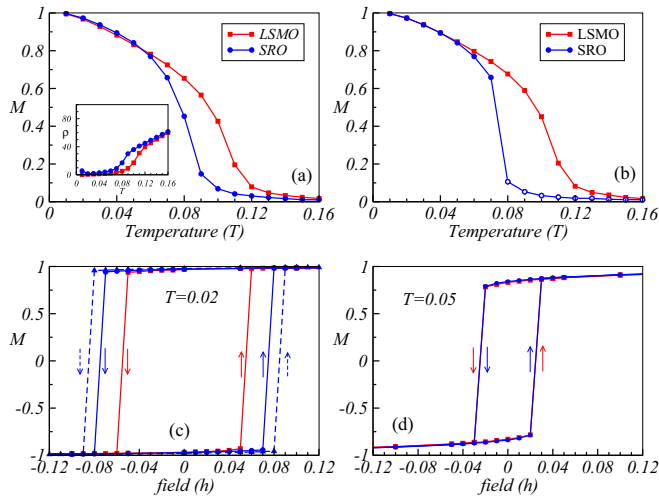

FIG. 2. The bulk properties of individual LSMO and SRO systems computed using the parameter sets listed in Table I. (a), (b) Magnetization M vs temperature T results with $A_{aniso}^{SRO} = 0.05$ in the whole temperature range and with $A_{aniso}^{SRO} = 0.05$ (0.00) below (above) T_C^{SRO}, respectively. In both cases, $T_C^{LSMO} > T_C^{SRO}$ with a reduced value of T_C^{SRO} for $A_{aniso}^{SRO} = 0.0$ above T_C^{SRO} case. Open symbol is used to represent the paramagnetic part of the SRO curve. Most of our calculations are performed for $T < T_C^{SRO}$ and we employ the parameters used in (a) to model LSMO and SRO in the rest of our calculations. Inset in (a) shows that both LSMO and SRO are metallic at low temperatures. (c), (d) M vs applied field h hysteresis loops of LSMO-like and SRO-like materials at low temperature $T = 0.02$ and moderate temperature $T = 0.05$, respectively. The arrows indicate the field sweep direction. Clearly, coercive field of SRO $H_C^{SRO} > H_C^{LSMO}$ at $T = 0.02$, but comparable to each other at $T = 0.05$. Also, we show the M-h hysteresis loop for SRO like materials for $A_{aniso}^{SRO} = 0.07$ in (c) using dashed lines. Legends are same in (a), (c), and (d).

effect. So, taking $A_{aniso}^{SRO} = 0$ above T_C and $A_{aniso}^{SRO} = 0.05$ below T_C, and keeping all other parameters fixed as in Fig. 2(a), we present the calculations for SRO in Fig. 2(b). Now, T_C^{SRO} is reduced and, consequently, the gap between the ferromagnetic transition temperatures of two systems widens, which is a better match to the experimental results. In this paper, most of the calculations are carried out below the ferromagnetic T_C of SRO (T_C^{SRO}), and by high temperature we mean $T \lesssim T_C^{SRO}$, similar to experiments. In that spirit, we use the parameter space employed in Fig. 2(a) for both LSMO and SRO to avoid confusion. In the inset of Fig. 2(a), we show the resistivity for both systems. We obtain the resistivity by calculating the dc limit of the conductivity as determined by the Kubo-Greenwood formula [92–94]. Our calculations show that both systems are metallic at low temperature, which agrees with the experimental results.

Next, we compare the coercive field H_C of both systems in Fig. 2(c). Our calculations show that $H_C^{LSMO} < H_C^{SRO}$ at low temperature ($T = 0.02$), giving rise to a combination of hard and soft FMs, as required for modeling the SL. On the other hand, H_C^{LSMO} is comparable to H_C^{SRO} at intermediate temperatures [see Fig. 2(d)] as we move close to T_C^{SRO}. So, the two sets of parameters that we assigned to LSMO-like and SRO-like materials qualitatively capture the essential physics that is required to investigate their SLs. Hence, we call them LSMO and SRO in our further analysis. What would happen to the M-h curve if we take a larger anisotropy constant $A_{aniso}^{SRO} = 0.07$ instead of $A_{aniso}^{SRO} = 0.05$, particularly at low temperatures? Obviously, H_C^{SRO} gets enhanced further, as shown using the dotted line in Fig. 2(c).

In the low-temperature magnetic hysteresis experiments of LSMO/SRO SLs, the magnetization of the SRO layer is pinned up to moderate field strength for a positive field cooled system, whereas LSMO layer switches its orientation during field sweep. This is a consequence of the higher coercive field of SRO as compared to LSMO. In addition, a positive EB is also observed in experiments below T_C^{SRO}, which is believed to be a consequence of antiferromagnetic interlayer coupling [56]. In fact, this antiferromagnetic interlayer coupling plays a significant role in the transport and magnetic properties of the LSMO/SRO SLs. Here, it is an interesting scenario where interlayer coupling turns out to be antiferromagnetic, although the constituent layers themselves have dominant ferromagnetic interactions among the core spins. This is explained using the transformed interfacial bond arrangements and resulting interfacial charge transfer. Density functional calculations suggest that the bond angle Mn–O–Ru at the interface drives an antiferromagnetic superexchange coupling [56,63], whose strength would be different from the superexchange interaction within either layer. The impact of interfacial electronic charge transfer is twofold: (i) it modifies the antiferromagnetic superexchange interaction and (ii) induces an antiferromagnetic interaction via carrier driven process at the interface, as discussed earlier. This charge carrier mediated coupling very much depends upon the modified hopping parameter t_I at the interface. In fact, the strength of charge transfer driven antiferromagnetic coupling would be larger for $t_I = t_{Mn} = 1$ as compared to that of $t_I = t_{Ru} = 0.5$.
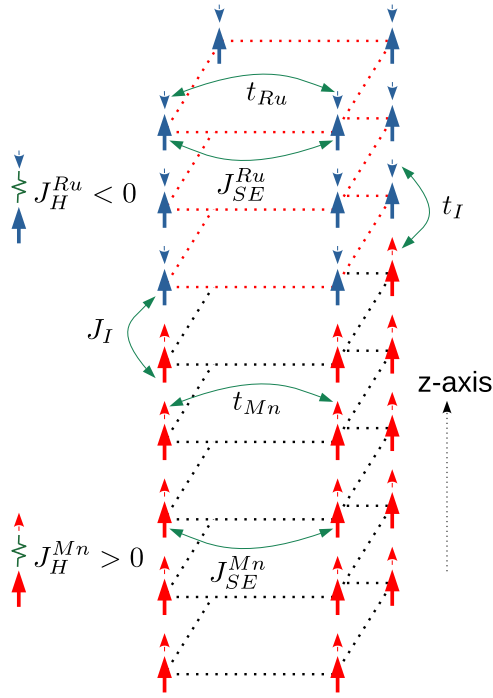
FIG. 3. Schematic of the lattice model for 5/3 LSMO/SRO superlattice based on Mn and Ru ions showing the hopping parameters (t_{Mn}, t_{Ru}, t_I), superexchange interactions (J_{SE}^{Mn}, J_{SE}^{Ru}, J_I), and Hund's couplings (J_H^{Mn}, J_H^{Ru}).

V. ESTABLISHING THE ANTIPARALLEL ALIGNMENT OF LSMO AND SRO LAYERS

It is generally assumed that the interlayer coupling decides the overall properties of heterostructures. So, we start the SL structure calculations by understanding the nature of interfacial interaction in 5/3 and 4/4 SLs. These notions of SL structures have already been discussed. Schematic of the lattice model for 5/3 LSMO/SRO SL showing the hopping parameters (t_{Mn}, t_{Ru}, t_I), superexchange interactions (J_{SE}^{Mn}, J_{SE}^{Ru}, J_I), and Hund's couplings (J_H^{Mn}, J_H^{Ru}) is shown in Fig. 3. To maintain the desired electron densities in both layers, one has to choose the relative on-site potential ϵ accordingly. ϵ takes the value Δ (0) in the LSMO (SRO) layer. And, we found that for $\Delta = 10.7$, LSMO and SRO layers maintain the electron densities 0.7 and 0.5, respectively, in both 5/3 SL and 4/4 SL systems. LSMO and SRO layers are coupled at the interface via hopping parameter t_I and superexchange interaction J_I. We set $t_I = 0.75$ and $J_I = 0$ unless otherwise mentioned. This will help us to first analyze the effects of carrier driven interfacial antiferromagnetic coupling. In subsequent calculations, the consequences of superexchange coupling is emphasized wherever necessary.

We measure the magnetization of 5/3 and 4/4 SLs by cooling from high temperature $T = 0.16$ in a very small external field $h = 0.002$ [see Fig. 4(a)]. In both cases, the magnetization starts to increase at $T \sim 0.11$, which is attributed to the ferromagnetic alignment of the high T_C constituent LSMO layer. At $T \sim 0.09$, the magnetization decreases for 4/4 SL, whereas the slope of the magnetization curve changes abruptly in the case of 5/3 SL. These results indicate that
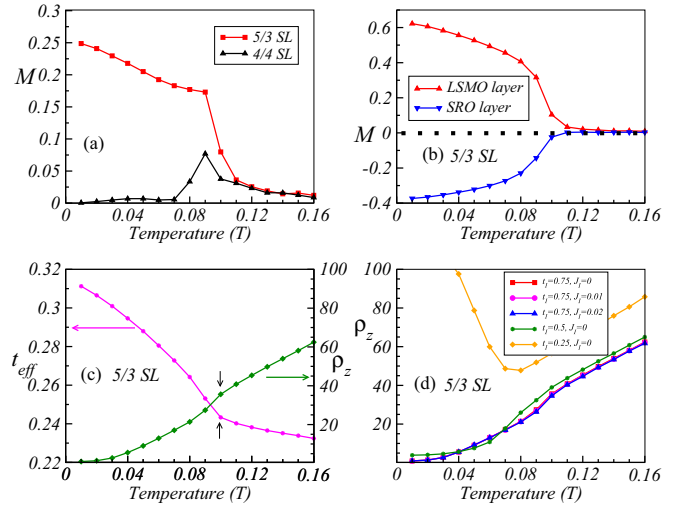

FIG. 4. Magnetic and transport properties of LSMO/SRO SLs: (a) Variation of M with T for 5/3 and 4/4 SLs showing the sign of onset of interfacial antiferromagnetic alignment at $T \sim 0.09$. (b) M vs T of individual LSMO and SRO layers for 5/3 SL confirms the fact that at low temperatures, both layers are ferromagnets but coupled antiferromagnetically to each other. (c) Variation of out-of-plane resistivity ρ_z with temperature for 5/3 SL shows an insulator-metal transition at $T = 0.1$. Also shown, the effective hopping parameter t_{eff}, where the sharp change at the same temperature is due to the gain in the kinetic energy of carriers in the SL. This corroborates the fact that antiferromagnetic interfacial coupling [shown in (b)] enhances the kinetic energy and drives the system towards a metallic phase. (d) Variation of ρ_z vs T for different combinations of interfacial hopping parameter and interfacial superexchange interaction (t_I, J_I) values depict that suppressed carrier hopping across the interface ($t_I = 0.25$) negates the insulator-metal transition.

the SRO layer starts to align ferromagnetically but in opposite orientation to the LSMO layer at $T = 0.09$. To verify this fact, we plot the magnetization of embedded LSMO and SRO layers separately for 5/3 SL in Fig. 4(b), which we found to be consistent with the results presented in Fig. 4(a). So, the antiferromagnetic interaction at the interface drives the layers to align antiferromagnetically at low temperatures. Now the question arises: Does this antiferromagnetic alignment at $T \sim 0.09$ lead to a metallic state according to our hypothesis, presented earlier, where we argued that antiferromagnetic alignment at the interface facilitate the delocalization of charge carriers? To check this, we calculated the out-of-plane resistivity $\rho_z(T)$ presented in Fig. 4(c). The resistivity depicts an insulator-metal transition around $T \sim 0.1$ (indicated by black arrow), where both layers start to align antiferromagnetically with each other as shown in Figs. 4(a) and 4(b). This ensures that the LSMO/SRO SL systems with antiferromagnetic interfacial coupling are metallic in nature. To establish the correspondence between resistivity and gain in kinetic energy, we calculate the effective hopping [95,96]

$$t_{\text{eff}} = \left\langle \sum_{j,\sigma} (c_{j,\sigma}^\dagger c_{j+z,\sigma} + \text{H.c.}) \right\rangle$$

of 5/3 SL, where the angular brackets represent the expectation value. The t_{eff} vs temperature shows a sharp change at

$T = 0.1$ [see Fig. 4(c)], indicating that gain in kinetic energy of the SL system gets enhanced at the same temperature where both LSMO and SRO layers start to align antiferromagnetically. So, our $t_{\text{eff}}(T)$ and $\rho_z(T)$ results compliment each other.

To establish the fact that the carrier-driven antiferromagnetic coupling between the two ferromagnetic layers steers the SL towards a metallic (insulating) state when LSMO and SRO are aligned in an antiparallel (parallel) configuration, as seen in experiments, we calculate the magnetic and transport properties using different combinations of interfacial hopping parameter t_I and interfacial superexchange interactions J_I. For varying J_I with a fixed $t_I = 0.75$, we did not find any variation in the resistivity curve as shown in Fig. 4(d). But for small values of t_I (with fixed $J_I = 0$), the system does not go to a metallic state at low temperatures, although LSMO and SRO layers align antiferromagnetically (not shown in figure). This shows that a reasonable interfacial hopping that also drives the antiferromagnetic interaction is necessary to understand the magnetotransport properties of LSMO/SRO SLs.

VI. POSITIVE EXCHANGE BIAS

We have established the essential properties of LSMO, SRO, and their SLs qualitatively. Now, we come to the key calculation of the paper, where we measure the magnetic hysteresis M-h loop. We start with 5/3 SL at low temperature $T = 0.02$. First, we cool down the SL from high temperature to $T = 0.02$ under an external magnetic field $h_{\text{cooling}} = +0.1$ and then measure the M-h loop. The field cycle of the h loop is restricted to ± 0.1, so the magnetization of the SRO layer remains in the up direction and does not flip at all. We will see in the next section that SRO flips its direction beyond $h = -0.1$. Here, the aim is to analyze the minor hysteresis loop of the SL, which is the full hysteresis loop of the embedded LSMO layer. We have presented the variation of magnetization of LSMO layer in Fig. 5(a). For $h = +0.1$, LSMO and SRO layers are aligned ferromagnetically along the field direction. As we decrease the magnetic field strength, the magnetization of LSMO layer flips its direction at a small +ve field (LSMO ↑ SRO ↑ to LSMO ↓ SRO ↑). Primarily, there are two reasons for this flip: (i) the coercive field of LSMO is smaller than SRO ($H_C^{\text{LSMO}} < H_C^{\text{SRO}}$), as shown in Fig. 2(c), and (ii) the interfacial antiferromagnetic coupling that wins over the low field strength in aligning the LSMO layer in its favor. While sweeping back the field from $h = -0.1$, a higher field strength ($h = 0.07$) is required to overcome the antiferromagnetic interlayer coupling and flip back the LSMO magnetization along the field direction. As a result, the hysteresis loop of the LSMO layer shifts towards the positive field axis, giving rise to a positive EB. In addition, we have calculated the spin-resolve density of states (DOS) at the Fermi level (ε_F) of the LSMO layer and plotted the spin up density of states $D_\uparrow^{\text{LSMO}}(\varepsilon_F)$ in Fig. 5(b), which perfectly follows the LSMO magnetic hysteresis loop shown in Fig. 5(a). This shows that if the carriers are perfectly aligned to the core spins, then the DOS of the soft FM can be used as a parameter to track the magnetization flipping in LSMO/SRO like SLs.

It has already been discussed that the carriers will be more delocalized (localized) across the interface in SL structures when the magnetic moments in LSMO and SRO layers are
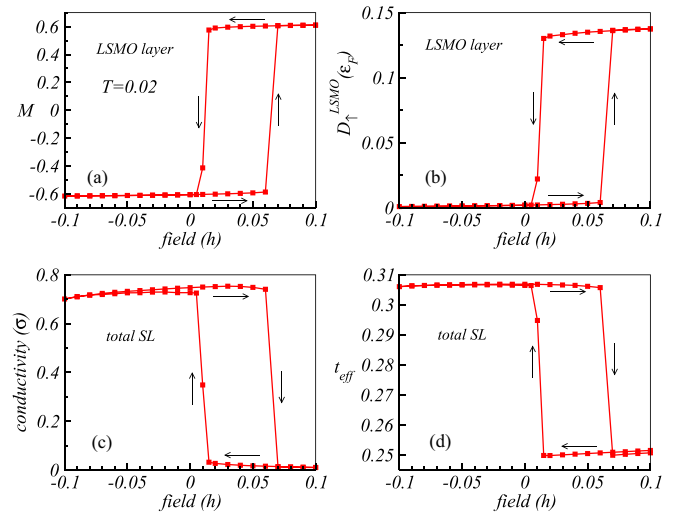

FIG. 5. Focuses on the minor hysteresis loops (hysteresis of only LSMO layer) of 5/3 SL at low temperature $T = 0.02$. Here, the applied field is restricted within a region such that only the magnetization of LSMO flips its direction, leaving the SRO layer pinned along up direction. The arrows indicate the field sweep direction. (a) The positive exchange bias of the soft magnetic layer LSMO with a shift of M-h hysteresis loop to the right of the zero field axis. (b) The hysteresis of spin-up density of states of LSMO layer at the Fermi level [$D_\uparrow^{\text{LSMO}}(\varepsilon_F)$], which follows magnetic hysteresis curve shown in (a). (c) Hysteresis of conductivity shows that the SL is more conducting for oppositely oriented LSMO and SRO layers as compared to their parallel configuration. (d) Hysteresis of effective hopping parameter t_{eff} follows conductivity loop which corroborates the fact that the carriers are more mobile in antiparallel configuration as compared to the parallel configuration of both layers across the interface.

aligned antiferromagnetically (ferromagnetically) with each other. To check this fact, we have calculated the dc conductivity throughout the magnetic hysteresis loop and found that the SL is more conducting in the antiparallel configuration as compared to the parallel configuration of LSMO and SRO layers, as shown in Fig. 5(c). We have also shown that the hysteresis loop of the effective hopping t_{eff} [see Fig. 5(d)] is very similar to the conductivity hysteresis loop, corroborating the fact that carriers are more mobile across the interface in an antiparallel configuration (LSMO ↓ SRO ↑) as compared to parallel orientation (LSMO ↑ SRO ↑).

VII. INVERTED HYSTERESIS LOOP

We now investigate the full hysteresis loop of the 5/3 SL at low temperature $T = 0.02$. Here and in later sections, all the calculations are carried out after cooling down the SL in external field $h_{\text{cooling}} = +0.15$, which is higher than H_C^{SRO}. At this forward saturation field strength, the magnetizations of both LSMO and SRO layers are aligned parallel to the external field. It is also important to remember that the SRO layer (LSMO layer) acts as a hard (soft) FM at $T = 0.02$. So, by decreasing the field from $h = +0.15$ towards $h = -0.15$, first, the LSMO layer reverses its magnetization at small but finite positive fields, giving rise to a negative remanence.
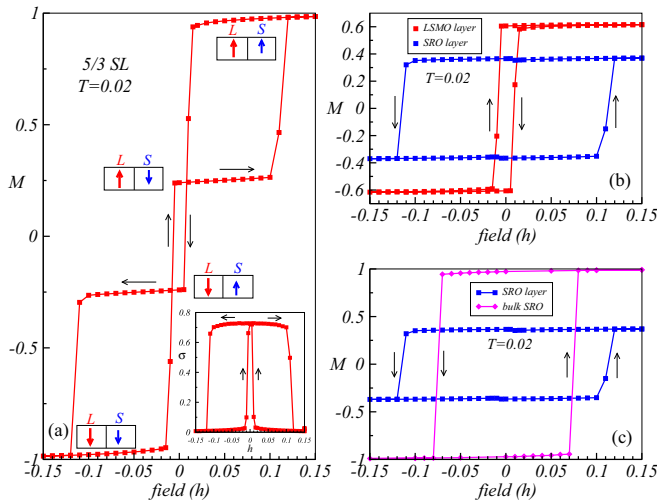
FIG. 6. Magnetotransport properties along the magnetic hysteresis measurements for 5/3 SL at $T = 0.02$: (a) The complete magnetic hysteresis curve shows a centrally inverted hysteresis loop with negative coercivity and negative remanence as observed in the experiment [62]. Relative magnetizations of LSMO and SRO layers (LSMO as L and SRO as S) are illustrated schematically. Inset shows that the conductivity in antiparallel configuration is larger than that of the parallel configuration along the hysteresis loop. (b) Separate plots of magnetic hysteresis curves of the embedded SRO and LSMO layers depict that SRO magnetization behaves conventionally, in contrast to LSMO magnetization, which is inverted. (c) The magnetic hysteresis of the embedded SRO layer is compared with that of the freestanding bulk system [replotted as in Fig. 2(c)]. The coercive field H_C of embedded SRO layer is larger than that of the bulk SRO due to the interfacial coupling, which resists the layer to flip at $H_C^{\text{SRO(bulk)}}$.

Then the SRO layer flips its magnetization at a larger external magnetic field of opposite polarity (at $h \sim -0.11$), as shown in Fig. 6(a). Now, traversing the field back from $h = -0.15$, the LSMO magnetization flips first at a small negative field, resulting in a negative remanence, and then SRO flips at a higher positive field (at $h \sim 0.11$) strength, giving rise to a central IHL, which is very similar to the experimental results [62]. For clarity, we have also plotted the magnetic hysteresis of individual LSMO and SRO layers embedded in SL in Fig. 6(b). The SRO layer shows a conventional hysteresis loop, whereas the LSMO layer depicts an inverted loop. This is because the interfacial antiferromagnetic coupling steers the LSMO layer to align opposite of the field direction by overcoming the external field energy to establish the antiferromagnetic configuration. So, the full M-h hysteresis loop at low temperature reveals the striking magnetization reversal process that is absent in the minor hysteresis loop of the SL presented in previous section. The SL system is found to be metallic (insulating) along the hysteresis loop where LSMO and SRO are aligned in an antiparallel (parallel) configuration as shown in the inset of Fig. 6(a). This fact is in good agreement with experimental results [90].

In addition, we compared the magnetic hysteresis of the embedded SRO layer with the bulk SRO system at $T = 0.02$ in Fig. 6(c). The coercive field of SRO in the SL is larger than that of the bulk SRO, $H_C^{\text{SRO(SL)}} > H_C^{\text{SRO(bulk)}}$. The earlier
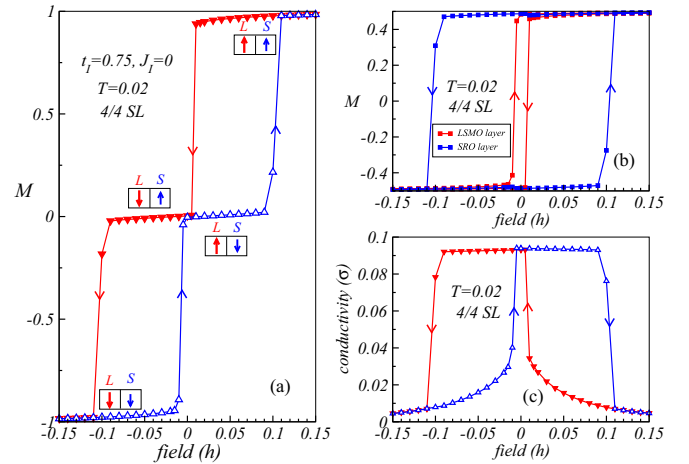
FIG. 7. Magnetotransport properties along the magnetic hysteresis measurements for 4/4 SL at $T = 0.02$: (a) The complete magnetic hysteresis curve where closed (open) symbol is used to plot the forward (reverse) field-sweeping direction. Relative orientations of magnetizations of LSMO and SRO layers (LSMO as L and SRO as S) are illustrated schematically. (b) Magnetic hysteresis curve of the embedded LSMO depicts an inverted loop, whereas in the case of SRO it is conventional. The centrally inverted hysteresis loop is not apparent in (a) as the magnetization of 4/4 SL system is vanishingly small for the AF alignment of LSMO and SRO layers [see Fig. 4(a)]. (c) The conductivity in antiparallel configuration is larger than that of the parallel configuration along the hysteresis loop. Legends are same in (a) and (c).

flipping of LSMO layer as shown in Fig. 6(a) favors the interfacial antiferromagnetic coupling which opposes the SRO layer to flip in the field direction up to a certain field strength that is larger than $H_C^{\text{SRO(bulk)}}$. As a result, relatively a large field of opposite polarity is required to flip the SRO layer as compared to its bulk counterpart.

Next, we present the magnetotransport properties along the magnetic hysteresis measurements for 4/4 SL at $T = 0.02$ using the protocol discussed above for 5/3 SL. It can be seen that the LSMO (SRO) layer depicts the inverted (conventional) hysteresis loop [Figs. 7(a) and 7(b)] as in the case of 5/3 SL. But, here, the central inverted part is not noticeable in Fig. 7(a) as the magnetization of 4/4 SL system is vanishingly small for the antiferromagnetic (AF) alignment of LSMO and SRO layers [see Fig. 4(a)]. Further, the 4/4 SL is more conducting in the antiparallel configuration as compared to the parallel configuration [Fig. 7(c)], similar to 5/3 SL. So, the overall flipping processes of both LSMO and SRO layers are very similar in 5/3 and 4/4 SL systems. Hence, all further calculations are done for 5/3 SL unless otherwise specified.

It is apparently clear that the central inverted part of the hysteresis loop in 5/3 SL is observed due to the flipping of the LSMO layer at a positive field during the field sweep. Will there be any change in the central part of the IHL if we reduce the strength of ferromagnetism in the LSMO layer? To answer this, first, we compare the M-h hysteresis loops for two different Hund's coupling strengths ($J_H^{Mn} = 24$ and 16) for the LSMO layer as shown in Fig. 8(a). A lower Hund's coupling value makes the overall ferromagnetic strength of
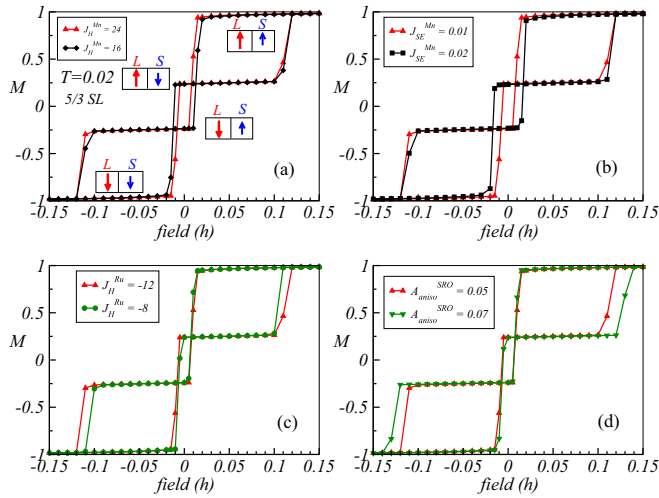
FIG. 8. Effects of ferromagnetic strength of LSMO and SRO layers on IHL of 5/3 SL at $T = 0.02$. Ferromagnetic strength is tuned by varying (a) J_H^{Mn} and (b) J_{SE}^{Mn} in LSMO, and (c) J_H^{Ru} and (d) $A_{\mathrm{aniso}}^{\mathrm{SRO}}$ in SRO. In both (a) and (b), the central part of the hysteresis loop becomes more prominent with decreasing the ferromagnetic strength in LSMO, while it remains unaffected by varying the ferromagnetic strength of SRO as shown in (c) and (d). Only the parameters given in the legends are varied, keeping all other parameters fixed (see Table I). The variation of parameters are chosen in such a way that the relative properties of LSMO and SRO presented in Sec. IV remain intact.

the LSMO layer weaker. As a result, the LSMO layer flips at a larger positive field during the field sweep as compared to the case of the stronger Hund's coupling layer. Consequently, the inverted part of the hysteresis loop becomes wider and hence more pronounced in the case of $J_H^{\mathrm{Mn}} = 16$ as compared to $J_H^{\mathrm{Mn}} = 24$. Second, superexchange interaction J_{SE}^{Mn} suppresses the Hund's coupling generated ferromagnetism. So, the central IHL widens when we use $J_{SE}^{\mathrm{Mn}} = 0.02$ in place of $J_{SE}^{\mathrm{Mn}} = 0.01$, as shown in Fig. 8(b).

Now we will check the effect of ferromagnetic strength of SRO layer on the central IHL of SL. The ferromagnetism in the SRO layer can be tuned by varying the values of the Hund's coupling J_H^{Ru} and the magnetocrystalline anisotropy $A_{\mathrm{aniso}}^{\mathrm{SRO}}$. The SRO layer flips its magnetization in a relatively lower field of opposite polarity ($h \sim -0.1$) for $J_H^{\mathrm{Ru}} = -8$ as compared to $h \sim -0.11$ for $J_H^{\mathrm{Ru}} = -12$, shown in Fig. 8(c). Next, if we increase the anisotropy from $A_{\mathrm{aniso}}^{\mathrm{SRO}} = 0.05$ to 0.07, only the SRO layer flips its magnetization at larger fields of opposite polarity [see Fig. 8(d)]. In both situations, whether we change the Hund's coupling strength or the anisotropy strength of the SRO layer, the central inverted part of the hysteresis loop remains unaffected. Therefore, our overall results show that the central inverted part of the hysteresis loop is mainly controlled by the LSMO layer of the SL system.

It was mentioned earlier that primarily there are two sources of interlayer antiferromagnetic interaction: (i) carrier-mediated antiferromagnetic coupling and (ii) Mn–O–Ru bond driven superexchange coupling (J_I). In all calculations presented till now, we incorporated only the first type of interaction among the core spins at the interface for
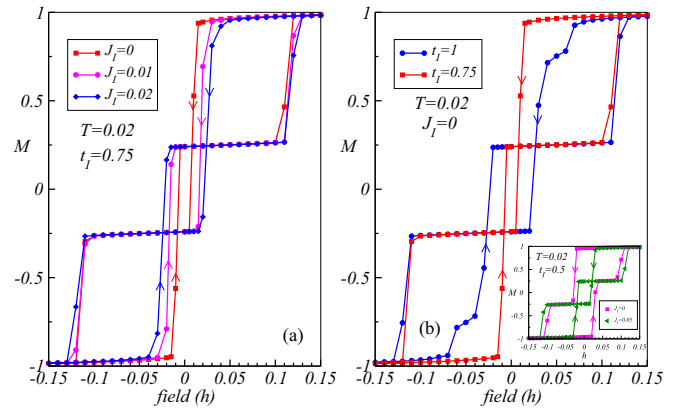

FIG. 9. Comparison of magnetic hysteresis loops of 5/3 SLs at $T = 0.02$ with (a) variation of the interfacial superexchange interaction J_I at fixed value of interfacial hopping parameter $t_I = 0.75$ and (b) variation of t_I at fixed $J_I = 0$. Both J_I and t_I enhance the interfacial coupling strength. So, the width of the central IHL broadened with increasing J_I and/or t_I. Inset: IHL is absent for the parameter set $(t_I, J_I) = (0.5, 0)$, which indicates that a reasonable strength of interfacial antiferromagnetic coupling is essential to realize the inverted hysteresis feature. In fact, for $(t_I, J_I) = (0.5, 0.05)$, an IHL is observed.

analyzing the hysteresis loop. Now we consider both interactions and investigate the IHL in Fig. 9 to emphasize the effect of Mn–Ru direct superexchange coupling. We compare the *M-h* hysteresis loops for different superexchange coupling strengths $J_I = 0$, 0.01, and 0.02 at fixed $t_I = 0.75$ at low temperature $T = 0.02$ in Fig. 9(a). The central inverted part of the hysteresis loop is seen to be more prominent for $J_I = 0.02$. The reason is the enhancement of overall (effective) antiferromagnetic interaction at the interface that facilitates the rotation of magnetization (from up to down direction) of LSMO layer at a larger positive applied field. The carrier-mediated antiferromagnetic coupling can also be enhanced (for fixed $J_I = 0$) by increasing the interlayer hopping parameter t_I to 1 instead of 0.75, which can be understood from the inverted part of the hysteresis loop shown in Fig. 9(b). The interlayer coupling strength decreases considerably in the case of suppressed carrier hopping $t_I = 0.5$ (keeping $J_I = 0$), which results in a conventional hysteresis loop without any inverted part [see inset of Fig. 9(b)]. The IHL is recovered for $t_I = 0.5$ and $J_I = 0.05$. These results clearly show the crucial role of interfacial antiferromagnetic coupling in generating the central IHL.

Next, we demonstrate the stability of the inverse hysteresis loop for different system sizes. Figure 10(a) shows the *M-h* hysteresis loops for four different system sizes, namely, N = $6 \times 6 \times 8$, $8 \times 8 \times 8$, $10 \times 10 \times 8$, and $12 \times 12 \times 8$ at low temperature $T = 0.02$. Here we have modified only the size of the planes, keeping the thickness of the SLs and individual layers fixed. So, all these calculations are for different sizes but each one of them falls under the 5/3 SL group. Interestingly, the overall hysteresis loops, including the central inverted parts, are hardly distinguishable from each other for all four cases. This shows that the magnetic properties we discussed for the system size N = $10 \times 10 \times 8$ remain
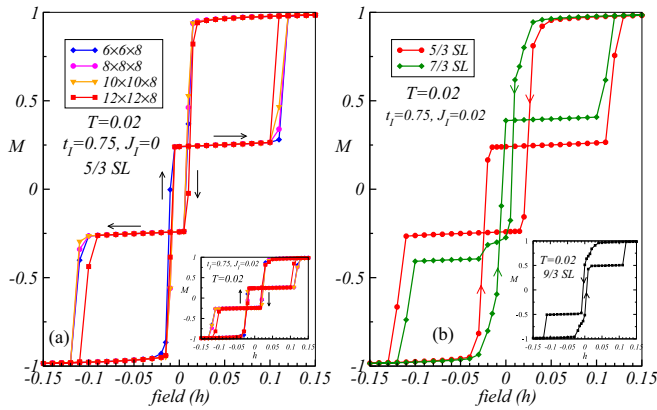
FIG. 10. The stability of IHL with different system sizes: (a) Magnetic hysteresis along with the IHLs for four different system sizes are seen to be almost indistinguishable from each other. All systems belong to the 5/3 SL structure. Inset: The IHLs are also stable for $J_I = 0.02$. (b) The shrinking of the width of IHL for 7/3 SL structure (system size $10 \times 10 \times 10$) as compared to 5/3 SL is due to thicker LSMO layer (seven planes), which flips its magnetization at a lower applied field strength as compared to thinner LSMO layer (five planes). Inset: IHL disappears for 9/3 SL (system size $10 \times 10 \times 12$).

very robust, without any significant size effect. We have also shown that the magnetic hysteresis loop remains unaffected by varying the size of the system for $J_I = 0.02$ [see the inset of Fig. 10(a)].

Switching LSMO moments within small magnetic field strengths results in the IHL for 5/3 SL at $T = 0.02$ and $J_I = 0$, discussed in Fig. 6. Tuning on the interlayer superexchange antiferromagnetic interaction ($J_I = 0.02$), the central IHL becomes more prominent (see Fig. 9). What will happen to the central IHL if one varies the thickness of LSMO layer, keeping SRO thickness fixed? To check this, we considered (i) 7/3 SL with a $10 \times 10 \times 10$ lattice and (ii) 9/3 SL with a $10 \times 10 \times 12$ lattice for $J_I = 0.02$. Keeping the thickness of the SRO layer fixed, if we increase the LSMO layer thickness it is clearly visible that the area of the central inverted loop part shrinks [see Fig. 10(b)]. If we further increase it, then the IHL vanishes and the conventional loop reappears for 9/3 SL [see inset of Fig. 10(b)]. In this case, the magnetization of the LSMO layer flips below $h = 0$, resulting in the disappearance of the IHL. This is because the thick LSMO layer does not prefer to get rotated easily (rotation is based on the interfacial antiferromagnetic coupling) as compared to the thin LSMO layer against the magnetic field energy. These results indicate the importance of relative thicknesses of the constituent layers to realize the IHL in SLs.

VIII. UNCONVENTIONAL THREE-STEP FLIPPING PROCESS OF MAGNETIZATION

The temperature-dependent hard or soft nature of LSMO and SRO results in unconventional and interesting magnetic hysteresis loops in LSMO/SRO SLs. We have calculated and discussed, in detail, the hysteresis loop at low temperatures where the coercive fields of LSMO and SRO layers are quite different from each other. What if the coercive fields of two
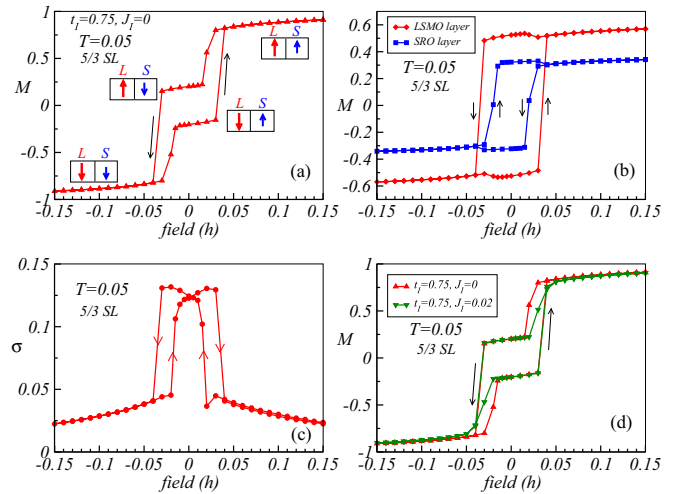

FIG. 11. Presents the magnetotransport properties of 5/3 SL at intermediate temperature $T = 0.05$, where the coercive fields of bulk LSMO and SRO are comparable to each other [see Fig. 2(d)]. We set $J_I = 0$. (a) M-h hysteresis loop shows a two-step switching process, but without any central inverted part. (b) clarifies the switching process with separately plotted M-h data of embedded LSMO and SRO layers. (b) along with (a) ensure that the magnetization of SRO layer flips first, which is followed by LSMO layer. In fact, embedded SRO layer shows inverted hysteresis feature. (c) shows that conductivity in parallel orientation remains smaller than that in the antiparallel configuration along the M-h hysteresis loop. (d) Additional interfacial superexchange coupling $J_I = 0.02$ does not change the qualitative features of the two-step flipping process of M-h hysteresis loop.

materials are comparable to each other? How does the magnetic hysteresis loop behave in such a scenario? For this, we have to study the M-h loops at high temperatures. Before going on to analyze high-temperature calculations, it would be interesting to explore the intermediate temperature regime where the coercive fields of the constituent bulk materials are already comparable to each other [see Fig. 2(d) for $T = 0.05$]. Hence, we plot the M-h magnetic hysteresis curve for 5/3 SL at $T = 0.05$ in Fig. 11(a), which shows a two-step process as in the low-temperature case. In high field strength, both layers are aligned along the field direction. Sweeping from forward to reverse saturation field, the SRO layer flips first at a small +ve field creating a ferrimagnetic SL magnetization and ultimately both layers align along the field direction (LSMO ↑ SRO ↑ to LSMO ↑ SRO ↓ to LSMO ↓ SRO ↓) at saturation field. This flipping scenario is more clear in Fig. 11(b), where we have plotted the magnetization of individual LSMO and SRO layers. It is clear that the LSMO layer is the second one to switch its magnetization direction. In fact, the flips of only the SRO layer depict an IHL similar to the LSMO layer presented in Fig. 6(b) for low temperatures. The inverted part is not visible for the whole SL structure at $T = 0.05$ due to the smaller effective magnetic moment in SRO layer, which happens to flip first in this case. So, to visualize the central IHL, it is necessary that the higher moment layer should flip first and give a negative remanence. The dc conductivity in Fig. 11(c) shows that the conductivity in a parallel configuration remains smaller compared to the antiparallel configuration, similar to the low-temperature case. The two-step switching process as
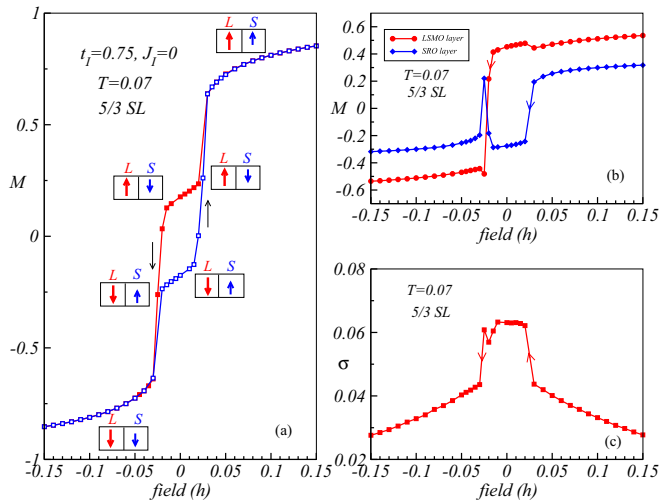
FIG. 12. Magnetotransport properties of 5/3 SL at high temperature $T = 0.07$ (close to T_C^{SRO}). (a) M-h hysteresis measurements depict the unconventional three-step magnetization flipping process, qualitatively similar to the experimental results [62]. Closed and open symbols are used to plot the forward and reverse field-sweeping directions, respectively. (b) The magnetization switching of the embedded individual LSMO and SRO layers during M-h cycle confirm the three-step flipping process. (c) Conductivity measurements along the hysteresis loop show that layers in the antiparallel configuration are more conducting than that in the parallel orientation, but their difference is reduced at high temperature as compared to low temperature.

FIG. 13. The effect of interfacial antiferromagnetic coupling on the three-step flipping process of 5/3 SL at high temperature $T = 0.07$. In (a), the interfacial superexchange interaction J_I is varied with keeping the interfacial hopping parameter fixed at $t_I = 0.75$, and in (b) t_I is varied with fixed $J_I = 0$. The interfacial coupling strength increases with increasing J_I and/or t_I. So, in both cases, the three-step flipping process is more prominent for higher values of J_I and t_I. Top inset: Magnetic switching remains as two-step process for $t_I = 0.5$ ($J_I = 0$) due to insufficient strength of the interfacial antiferromagnetic coupling. Bottom inset: The three-step flipping process is recovered for $t_I = 0.5$ and $J_I = 0.05$.

a function of the magnetic field remains intact even modifying the interlayer interaction by tuning on the superexchange mediated coupling to $J_I = 0.02$ [see Fig. 11(d)].

At both low and intermediate temperatures, a two-step switching process is observed. LSMO (SRO) flips first at $T = 0.02$ ($= 0.05$) and generates a ferrimagnetic configuration of the magnetic moments in SL in the intermediate step of the M-h hysteresis curve. But at high temperature, close to T_C^{SRO}, an unconventional three-step switching process (LSMO ↑ SRO ↑ to LSMO ↑ SRO ↓ to LSMO ↓ SRO ↑ to LSMO ↓ SRO ↓) is observed in experiments [62]. Here, the SRO layer flips first at a positive low field, followed by a switching of the overall ferrimagnetic SL magnetization in negative low fields and a further switching of the SRO layer to align along the field direction. To understand this complicated unconventional three-step process, we study the M-h hysteresis curve at $T = 0.07$ in Fig. 12(a). This temperature is just below the T_C of SRO, similar to the experimental setup. During the hysteresis measurements starting from $h = +0.15$, sweeping from forward to reverse saturation field, SRO layer switches its direction first, as in the case of $T = 0.05$, making the SL ferrimagnetic. This ferrimagnetic configuration changes its overall direction at $h \sim -0.025$. This flipping process allows the system to gain magnetic field energy by aligning the LSMO layer, which has larger magnetization among the two ferromagnetic layers, along the field direction, and keeping the interfacial antiferromagnetic interaction intact. Then, going further beyond this field strength, both layers orient in the field direction. The three-step flipping process
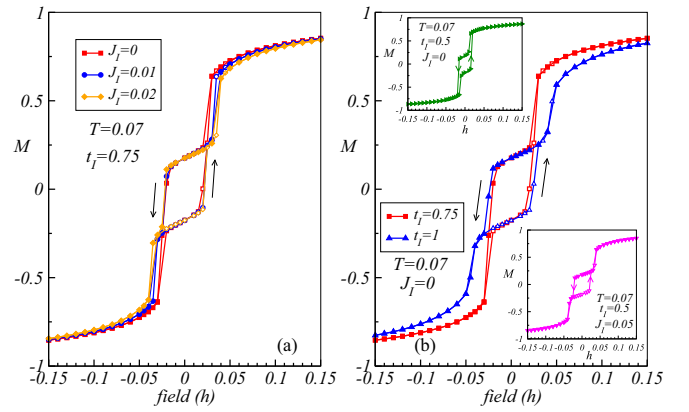
is also observed during traversing sweep from $h = -0.15$, which emphasizes the stability of both ferrimagnetic configurations (LSMO ↓ SRO ↑ and LSMO ↑ SRO ↓) along the hysteresis loop. This three-step flipping process is depicted in Fig. 12(b), where we have plotted the magnetization of the individual layers (plotted only for sweeping from the forward to the reverse saturation field). The carrier-mediated antiferromagnetic interaction at the interface for fixed $J_I = 0$ plays a vital role in stabilizing both ferrimagnetic phases, which we will discuss soon. It is also important to note here that, due to high operating temperature value, the saturation magnetizations of both layers are smaller than the saturation magnetization values observed in earlier calculations. Also, the dc conductivity in the parallel configuration is found to be only marginally smaller than the antiparallel configuration [see Fig. 12(c)].

In the three-step switching process [shown in Fig. 12(a)], although the reversal of ferrimagnetic SL configuration is observed, the second ferrimagnetic configuration (LSMO ↓ SRO ↑) withstands over a very narrow magnetic field window. To show that the interfacial antiferromagnetic interaction plays a significant role in stabilizing these ferrimagnetic phases, we incorporated the superexchange interaction and calculated the magnetic hysteresis loop of the SL at $T = 0.07$. The three-step switching process is found to be more prominent, particularly the second ferrimagnetic configuration (LSMO ↓ SRO ↑) for $J_I = 0.01$ and 0.02 as shown in Fig. 13(a). This indicates that the LSMO layer prefers to orient along the field direction at a particular small negative field value for which the ferrimagnetic SL configuration reverses to maintain the antiferromagnetic interaction between two layers at the interface. This is also supported from the results obtained from varying the interlayer hopping parameter t_I

with fixed $J_I = 0$. As the carrier-driven antiferromagnetic coupling at the interface increases with t_I, the three-step magnetic flipping process is more prominent for $t_I = 1$ as compared to $t_I = 0.75$ [see Fig. 13(b)]. But, interestingly, the magnetic switching remains a two-step process for $t_I = 0.5$ due to insufficient strength of the interfacial antiferromagnetic coupling as shown in the top inset of Fig. 13(b). Here, if we incorporate a large superexchange interaction ($J_I = 0.05$), then only the three-step flipping process is recovered [see bottom inset of Fig. 13(b)]. These results establish that a reasonable strength of interfacial antiferromagnetic coupling (comprised of carrier driven and bond driven) between LSMO and SRO is required to realize the three-step switching process at high temperature, as seen in experiments.

IX. CONCLUSIONS

In this paper, we investigated the interfacial antiferromagnetic interaction driven complex magnetotransport phenomena observed in LSMO/SRO SLs within a one-band double-exchange model using a Monte Carlo technique based on the traveling cluster approximation. We considered the appropriate magnetocrystalline anisotropy interaction and superexchange interactions terms of the constituent materials LSMO and SRO in the model Hamiltonian. Also, our calculations incorporate (i) the carrier-driven and (ii) the

bond-mediated superexchange interfacial antiferromagnetic interactions between Mn and Ru to demonstrate the vital role of interfacial coupling in deciding the magnetotransport properties along hysteresis loop. Our conductivity calculations show that the antialigned core spins at the interface prompt carrier hopping between the layers to gain kinetic energy and consequently steers the SL system towards a metallic (less resistive) phase. On the other hand, the SL is found to be in a less metallic or insulating state when LSMO and SRO layers are aligned along the same direction. Hence, the system undergoes a metal-insulator or insulator-metal transition upon varying the temperature and/or the applied magnetic field. Interestingly, by invoking the antiferromagnetic coupling at the interface, we explained the EB effect and IHL at low temperatures, and unconventional three-step flipping mechanism at high temperatures (close to ferromagnetic T_C of SRO), which are in good agreement with the experimental results. In addition, our calculations establish that the carrier-driven antiferromagnetic interaction is one of the necessary ingredients to understand the one-to-one correlation between magnetic and transport properties of LSMO/SRO SLs observed in experiments.

[1] J. B. Goodenough, Chem. Mater. **26**, 820 (2014).

[2] D. I. Khomskii, J. Magn. Magn. Mater. **306**, 1 (2006).

[3] P. Zubko, S. Gariglio, M. Gabay, P. Ghosez, and J. M. Triscone, Annu. Rev. Condens. Matter Phys. **2**, 141 (2011).

[4] H. Y. Hwang, Y. Iwasa, M. Kawasaki, B. Keimer, N. Nagaosa, and Y. Tokura, Nat. Mater. **11**, 103 (2012).

[5] J. Mannhart and D. G. Schlom, Science **327**, 1607 (2010).

[6] M. Fiebig, T. Lottermoser, D. Meier, and M. Trassin, Nat. Rev. Mater. **1**, 16046 (2016).

[7] K. F. Wang, J. M. Liu, and Z. F. Ren, Adv. Phys. **58**, 321 (2009).

[8] N. Feng, W. Mi, X. Wang, Y. Cheng, and U. Schwingenschlogl, ACS Appl. Mater. Interfaces **7**, 10612 (2015).

[9] S. M. Wu, S. A. Cybart, P. Yu, M. D. Rossell, J. X. Zhang, R. Ramesh, and R. C. Dynes, Nat. Mater. **9**, 756 (2010).

[10] P. Yu, J. S. Lee, S. Okamoto, M. D. Rossell, M. Huijben, C. H. Yang, Q. He, J. X. Zhang, S. Y. Yang, M. J. Lee, Q. M. Ramasse, R. Erni, Y. H. Chu, D. A. Arena, C. C. Kao, L. W. Martin, and R. Ramesh, Phys. Rev. Lett. **105**, 027201 (2010).

[11] A. P. Ramirez, J. Phys.: Condens. Matter **9**, 8171 (1997).

[12] F. Y. Bruno, J. Garcia-Barriocanal, M. Varela, N. M. Nemes, P. Thakur, J. C. Cezar, N. B. Brookes, A. Rivera-Calzada, M. Garcia-Hernandez, C. Leon, S. Okamoto, S. J. Pennycook, and J. Santamaria, Phys. Rev. Lett. **106**, 147205 (2011).

[13] J. Garcia-Barriocanal, J. C. Cezar, F. Y. Bruno, P. Thakur, N. B. Brookes, C. Utfeld, A. Rivera-Calzada, S. R. Giblin, J. W. Taylor, J. A. Duffy, S. B. Dugdale, T. Nakamura, K. Kodama, C. Leon, S. Okamoto, and J. Santamaria, Nat. Commun. **1**, 82 (2010).

[14] J. Hoffman, I. C. Tung, B. B. Nelson-Cheeseman, M. Liu, J. W. Freeland, and A. Bhattacharya, Phys. Rev. B **88**, 144411 (2013).

[15] C. He, A. J. Grutter, M. Gu, N. D. Browning, Y. Takamura, B. J. Kirby, J. A. Borchers, J. W. Kim, M. R. Fitzsimmons, X. Zhai, V. V. Mehta, F. J. Wong, and Y. Suzuki, Phys. Rev. Lett. **109**, 197202 (2012).

[16] J. K. Murthy and P. S. Anil Kumar, Sci. Rep. **7**, 6919 (2017).

[17] A. Bhattacharya, Annu. Rev. Mater. Res. **44**, 65 (2014).

[18] P. Anil Kumar and D. D. Sarma, Appl. Phys. Lett. **100**, 262407 (2012).

[19] S. Emori, U. S. Alaan, M. T. Gray, V. Sluka, Y. Chen, A. D. Kent, and Y. Suzuki, Phys. Rev. B **94**, 224423 (2016).

[20] M. Wahler, N. Homonnay, T. Richter, A. Mueller, C. Eisenschmidt, B. Fuhrmann, and G. Schmidt, Sci. Rep. **6**, 28727 (2016).

[21] M. Gibert, P. Zubko, R. Scherwitzl, J. Iniguez, and J. Triscone, Nat. Mater. **11**, 195 (2012).

[22] G. Zhou, C. Song, Y. Bai, Z. Quan, F. Jiang, W. Liu, Y. Xu, S. S. Dhesi, and X. Xu, ACS Appl. Mater. Interfaces **9**, 3156 (2017).

[23] X. Ke, M. S. Rzchowski, L. J. Belenky, and C. B. Eom, Appl. Phys. Lett. **84**, 5458 (2004).

[24] W. H. Meiklejohn and C. P. Bean, Phys. Rev. **102**, 1413 (1956).

[25] J. Nogues and I. K. Schuller, J. Magn. Magn. Mater. **192**, 203 (1999).

[26] S. Mangin, F. Montaigne, and A. Schuhl, Phys. Rev. B **68**, 140404(R) (2003).

[27] J. Nogues, D. Lederman, T. J. Moran, and Ivan K. Schuller, Phys. Rev. Lett. **76**, 4624 (1996).

[28] Z. J. Guo, J. S. Jiang, J. E. Pearson, S. D. Bader, and J. P. Liu, Appl. Phys. Lett. **81**, 2029 (2002).

[29] R. Rana, P. Pandey, R. P. Singh, and D. S. Rana, Sci. Rep. **4**, 4138 (2014).

[30] J. Nogues, J. Sort, V. Langlais, V. Skumryev, S. Surinach, J. S. Munoz, and M. D. Baro, Phys. Rep. **422**, 65 (2005).

[31] M. Gruyters and D. Schmitz, Phys. Rev. Lett. **100**, 077205 (2008).

[32] P. Bruno, J. Phys.: Condens. Matter **11**, 9403 (1999).

[33] N. C. Koon, Phys. Rev. Lett. **78**, 4865 (1997).

[34] C. Binek, S. Polisetty, X. He, and A. Berger, Phys. Rev. Lett. **96**, 067201 (2006).

[35] F. Radu, R. Abrudan, I. Radu, D. Schmitz, and H. Zabel, Nat. Commun. **3**, 715 (2012).

[36] W. Zhang, A. Chen, J. Jian, Y. Zhu, L. Chen, P. Lu, Q. Jia, J. L. MacManus-Driscoll, X. Zhang, and H. Wang, Nanoscale **7**, 13808 (2015).

[37] M. Huijben, P. Yu, L. W. Martin, H. J. A. Molegraaf, Y. H. Chu, M. B. Holcomb, N. Balke, G. Rijnders, and R. Ramesh, Adv. Mater. **25**, 4739 (2013).

[38] M. Bibes, J. E. Villegas, and A. Barthelemy, Adv. Phys. **60**, 5 (2011).

[39] M. Ziese and I. Vrejoiu, Phys. Status Solidi RRL **7**, 243 (2013).

[40] M. Saghayezhian, S. Kouser, Z. Wang, H. Guo, R. Jin, J. Zhang, Y. Zhu, S. T. Pantelides, and E. W. Plummer, Proc. Natl. Acad. Sci. USA **116**, 10309 (2019).

[41] P. Ghising, B. Samantaray, and Z. Hossain, Phys. Rev. B **101**, 024408 (2020).

[42] S. Esho, Jpn. J. Appl. Phys. **15**, 93 (1976).

[43] A. Banerjee, J. Sannigrahi, S. Giri, and S. Majumdar, Phys. Rev. B **98**, 104414 (2018).

[44] P. J. H. Bloemen, H. W. van Kesteren, H. J. M. Swagten, and W. J. M. de Jonge, Phys. Rev. B **50**, 13505 (1994).

[45] S. Sabet, A. Moradabadi, S. Gorji, M. H. Fawey, E. Hildebrandt, I. Radulov, D. Wang, H. Zhang, C. Kubel, and L. Alff, Phys. Rev. Appl. **11**, 054078 (2019).

[46] E. E. Fullerton, J. S. Jiang, and S. D. Bader, J. Magn. Magn. Mater. **200**, 392 (1999).

[47] S. C. Das, K. Mandal, P. Dutta, S. Pramanick, and S. Chatterjee, Phys. Rev. B **100**, 024409 (2019).

[48] S. Das, A. D. Rata, I. V. Maznichenko, S. Agrestini, E. Pippel, N. Gauquelin, J. Verbeeck, K. Chen, S. M. Valvidares, H. Babu Vasili, J. Herrero-Martin, E. Pellegrin, K. Nenkov, A. Herklotz, A. Ernst, I. Mertig, Z. Hu, and K. Dorr, Phys. Rev. B **99**, 024416 (2019).

[49] B. C. Behera, P. Padhan, and W. Prellier, J. Phys.: Condens. Matter **28**, 196004 (2016).

[50] S. Singh, J. T. Haraldsen, J. Xiong, E. M. Choi, P. Lu, D. Yi, X. D. Wen, J. Liu, H. Wang, Z. Bi, P. Yu, M. R. Fitzsimmons, J. L. MacManus-Driscoll, R. Ramesh, A. V. Balatsky, J. X. Zhu, and Q. X. Jia, Phys. Rev. Lett. **113**, 047204 (2014).

[51] B. Li, Rajesh V. Chopdekar, Alpha T. N'Diaye, A. Mehta, J. P. Byers, Nigel D. Browning, E. Arenholz, and Y. Takamura, Appl. Phys. Lett. **109**, 152401 (2016).

[52] P. Padhan, W. Prellier, and R. C. Budhani, Appl. Phys. Lett. **88**, 192509 (2006).

[53] P. Padhan and W. Prellier, Appl. Phys. Lett. **99**, 263108 (2011).

[54] S. Thota, Q. Zhang, F. Guillou, U. Laders, N. Barrier, W. Prellier, A. Wahl, and P. Padhan, Appl. Phys. Lett. **97**, 112506 (2010).

[55] Q. Zhang, S. Thota, F. Guillou, P. Padhan, A. Wahl, and W. Prellier, J. Phys.: Condens. Matter **23**, 052201 (2011).

[56] M. Ziese, I. Vrejoiu, E. Pippel, P. Esquinazi, D. Hesse, C. Etz, J. Henk, A. Ernst, I. V. Maznichenko, W. Hergert, and I. Mertig, Phys. Rev. Lett. **104**, 167203 (2010).

[57] J. H. Park, E. Vescovo, H.-J. Kim, C. Kwon, R. Ramesh, and T. Venkatesan, Nature (London) **392**, 794 (1998).

[58] M. Bowen, A. Barthelemy, M. Bibes, E. Jacquet, J. P. Contour, A. Fert, F. Ciccacci, L. Duo, and R. Bertacco, Phys. Rev. Lett. **95**, 137203 (2005).

[59] A. Urushibara, Y. Moritomo, T. Arima, A. Asamitsu, G. Kido, and Y. Tokura, Phys. Rev. B **51**, 14103 (1995).

[60] A. Kanbayasi, J. Phys. Soc. Jpn. **41**, 1879 (1976).

[61] A. J. Grutter, F. J. Wong, E. Arenholz, A. Vailionis, and Y. Suzuki, Phys. Rev. B **85**, 134429 (2012).

[62] M. Ziese, I. Vrejoiu, and D. Hesse, Appl. Phys. Lett. **97**, 052504 (2010).

[63] Y. Lee, B. Caes, and B. N. Harmon, J. Alloys Compd. **450**, 1 (2008).

[64] S. Kumar and P. Majumdar, Eur. Phys. J. B **50**, 571 (2006).

[65] K. Pradhan and A. P. Kampf, Phys. Rev. B **88**, 115136 (2013).

[66] E. Dagotto, T. Hotta, and A. Moreo, Phys. Rep. **344**, 1 (2001).

[67] Y. Tokura, Rep. Prog. Phys. **69**, 797 (2006).

[68] E. Dagotto, S. Yunoki, A. L. Malvezzi, A. Moreo, J. Hu, S. Capponi, D. Poilblanc, and N. Furukawa, Phys. Rev. B **58**, 6414 (1998).

[69] C. Zener, Phys. Rev. **82**, 403 (1951).

[70] S. Yunoki, J. Hu, A. L. Malvezzi, A. Moreo, N. Furukawa, and E. Dagotto, Phys. Rev. Lett. **80**, 845 (1998).

[71] K. Pradhan and P. Majumdar, Europhys. Lett. **85**, 37007 (2009).

[72] J. M. D. Coey, M. Viret, and S. von Molnar, Adv. Phys. **48**, 167 (1999).

[73] K. Steenbeck, T. Habisreuther, C. Dubourdieu, and J. P. Senateur, Appl. Phys. Lett. **80**, 3361 (2002).

[74] D. J. Singh, J. Appl. Phys. **79**, 4818 (1996).

[75] X. K. Ning, Z. J. Wang, and Z. D. Zhang, J. Appl. Phys. **117**, 093907 (2015).

[76] G. Koster, L. Klein, W. Siemons, G. Rijnders, J. S. Dodge, C. B. Eom, D. H. A. Blank, and M. R. Beasley, Rev. Mod. Phys. **84**, 253 (2012).

[77] S. N. Bushmeleva, V. Y. Pomjakushin, E. V. Pomjakushina, D. V. Sheptyakov, and A. M. Balagurov, J. Magn. Magn. Mater. **305**, 491 (2006).

[78] P. B. Allen, H. Berger, O. Chauvet, L. Forro, T. Jarlborg, A. Junod, B. Revaz, and G. Santi, Phys. Rev. B **53**, 4393 (1996).

[79] L. Klein, J. S. Dodge, C. H. Ahn, J. W. Reiner, L. Mieville, T. H. Geballe, M. R. Beasley, and A. Kapitulnik, J. Phys.: Condens. Matter **8**, 10111 (1996).

[80] J. M. Rondinelli, N. M. Caffrey, S. Sanvito, and N. A. Spaldin, Phys. Rev. B **78**, 155107 (2008).

[81] J. S. Dodge, E. Kulatov, L. Klein, C. H. Ahn, J. W. Reiner, L. Mieville, T. H. Geballe, M. R. Beasley, A. Kapitulnik, H. Ohta, Y. Uspenskii, and S. Halilov, Phys. Rev. B **60**, R6987(R) (1999).

[82] D. E. Shai, C. Adamo, D. W. Shen, C. M. Brooks, J. W. Harter, E. J. Monkman, B. Burganov, D. G. Schlom, and K. M. Shen, Phys. Rev. Lett. **110**, 087004 (2013).

[83] M. Kim and B. I. Min, Phys. Rev. B **91**, 205116 (2015).

[84] C. H. Chang, A. Huang, S. Das, H. T. Jeng, S. Kumar, and R. Ganesh, Phys. Rev. B **96**, 184408 (2017).

[85] D. Toyota, I. Ohkubo, H. Kumigashira, M. Oshima, T. Ohnishi, M. Lippmaa, M. Takizawa, A. Fujimori, K. Ono, M. Kawasaki, and H. Koinuma, Appl. Phys. Lett. **87**, 162508 (2005).

[86] L. Klein, J. S. Dodge, C. H. Ahn, G. J. Snyder, T. H. Geballe, M. R. Beasley, and A. Kapitulnik, Phys. Rev. Lett. **77**, 2774 (1996).

[87] J. M. Longo, P. M. Raccah, and J. B. Goodenough, J. Appl. Phys. **39**, 1327 (1968).

[88] A. Kanbayasi, J. Phys. Soc. Jpn. **41**, 1876 (1976).

[89] M. Ziese, I. Vrejoiu, and D. Hesse, Phys. Rev. B **81**, 184418 (2010).

[90] K. S. Takahashi, A. Sawa, Y. Ishii, H. Akoh, M. Kawasaki, and Y. Tokura, Phys. Rev. B **67**, 094413 (2003).

[91] S. Chakraborty, S. K. Das, and K. Pradhan, Phys. Rev. B **102**, 245112 (2020).

[92] G. D. Mahan, *Quantum Many Particle Physics* (Plenum, New York, 1990).

[93] S. Kumar and P. Majumdar, Europhys. Lett. **65**, 75 (2004).

[94] K. Pradhan and A. P. Kampf, Phys. Rev. B **87**, 155152 (2013).

[95] S. R. White, D. J. Scalapino, R. L. Sugar, E. Y. Loh, J. E. Gubernatis, and R. T. Scalettar, Phys. Rev. B **40**, 506 (1989).

[96] R. Mondaini and T. Paiva, Phys. Rev. B **95**, 075142 (2017).